

Hybrid Polyoxometalate Salt Adhesion by Butyltin Functionalization

Morgan Rose Olsen, Ian Colliard, Tasnim Rahman, Taiki C. Miyaishi, Bryan Harper, Stacey Harper, and May Nyman*



Cite This: *ACS Appl. Mater. Interfaces* 2021, 13, 19497–19506



Read Online

ACCESS |

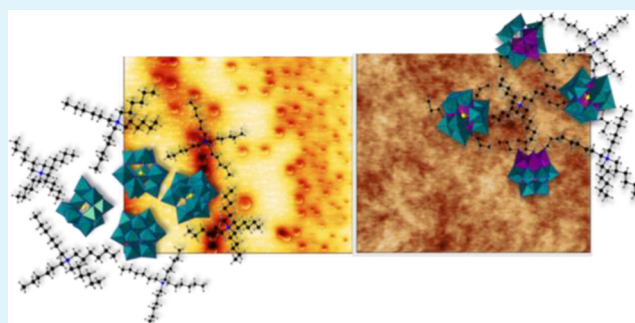
Metrics & More

Article Recommendations

Supporting Information

ABSTRACT: Polyoxometalate (POM)-based ionic liquids, with nearly infinite compositional variations to fine-tune antimicrobial and physical properties, function as water purification filters, anticorrosion/antibacterial coatings for natural stones, self-repairing acid-resistant coatings, catalysts, and electroactive, stable solvents. By combining hydrophobic quaternary ammonium cations (QACs; tetraheptylammmonium and trihexyltetradecylammonium) with butyltin-substituted polyoxotungstates $[(\text{BuSn})_3(\alpha\text{-SiW}_9\text{O}_{37})]$ via repeated solvent extraction-ion exchange, we obtained phase-pure hybrid POM salts (referred to as such because they melt above room temperature). If the solvent extraction process is performed only once, then solids with high salt contamination and considerably lower melting temperatures are obtained. Solution-phase behavior, based on POM–QAC interactions, was similar for all formulations in polar and nonpolar organic solvents, as observed by X-ray scattering and multinuclear magnetic resonance spectroscopy. However, solid thin films of the butyltin-functionalized hybrid POM salts were significantly more stable and adhesive than their inorganic analogues. We attribute this to the favorable hydrophobic interactions between the butyltin groups and the QACs. All synthesized hybrid POM salts display a potent antimicrobial activity toward *Escherichia coli*. These studies provide fundamental form-function understanding of hybrid POM salts, based on interactions between ions in these complex hybrid phases.

KEYWORDS: polyoxometalate, ionic liquids, biocidal, organotin, antimicrobial, quaternary ammonium



Solution-phase behavior, based on POM–QAC interactions, was similar for all formulations in polar and nonpolar organic solvents, as observed by X-ray scattering and multinuclear magnetic resonance spectroscopy. However, solid thin films of the butyltin-functionalized hybrid POM salts were significantly more stable and adhesive than their inorganic analogues. We attribute this to the favorable hydrophobic interactions between the butyltin groups and the QACs. All synthesized hybrid POM salts display a potent antimicrobial activity toward *Escherichia coli*. These studies provide fundamental form-function understanding of hybrid POM salts, based on interactions between ions in these complex hybrid phases.

INTRODUCTION

The interface between a solid and an aqueous or air medium creates an environment for microorganisms to attach to the surface and create biofilms. A biofilm is an assemblage of surface-associated microbial cells that are enclosed in an extracellular polymeric matrix. Biofilms lead to fouling of infrastructures, water treatment plants, manufacturing facilities, packaged foods, and medical implants, compromising health and promoting the transmission of infectious disease.¹ Biofilm formation motivates the design of antimicrobial surfaces, including multifunctional, hybrid organic–inorganic nanocomposites.^{2–8} In such composites, the inorganic components (usually nanoparticles) can lend antimicrobial, oxidative, and biomolecule-binding properties, while the organic components (usually polymers) provide hydrophobicity and biocidal properties. The efficacy of antimicrobial surfaces depends not only on the characteristics of each component but also on their emergent properties. Recently, Streb and co-workers have pioneered the design and optimization of polyoxometalate-based ionic liquids (POM-ILs) as antimicrobial coatings,^{9,10} which are, in one sense, molecular counterparts of the nanoparticle–polymer composites.^{11–13} POMs are anionic, inorganic metal oxide clusters that are stabilized in solution by counterions and have a wide range of structural topologies

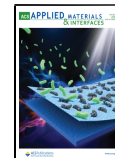
and chemical properties.¹⁴ Applications based on POM–biomolecule interactions have been realized, including antibacterial,¹⁵ antimicrobial,¹⁵ antiviral,¹⁶ antitumor,¹⁷ and antiamyloid fibril reagents (related to Alzheimer's disease).¹⁸ They have also been used for selective peptide hydrolysis¹⁹ and as a protein crystallization and structure elucidation aid.^{20–22} The counterions for POMs are most typically alkalis and alkylammonium, and interactions between the POMs and the counterion influence their physical properties including melting temperature and crystallization behavior.¹⁴

Quaternary ammonium counterions (QACs) engender POM-ILs with both physical and antibacterial properties suitable for antimicrobial coatings.^{10,23} Longer-chain QACs (i.e., $N(\text{C}_n\text{H}_{2n+1})_4^+$, $n \geq 4$) are able to disrupt cell wall lipid bilayers. In addition, the poor crystallization ability of these cations and the low melting temperature of the hybrid material

Received: February 18, 2021

Accepted: April 7, 2021

Published: April 15, 2021



enable a facile surface coating. POM-ILs have been constructed from Keggin and Dawson POMs ($[XM_{12}O_{40}]^{3/4-}$ and $[X_2M_{18}O_{62}]^{6/8-}$, respectively; $n = X = P, Si; M = Mo, W$), as well as the lacunary derivatives and transition-metal functionalized lacunary derivatives of the Keggin ion.⁹ Effective QACs include alkylammonium, alkylphosphonium, alkylpyridinium, or imadazolium.^{9,10} The antimicrobial activity of QACs has generally been correlated with the N-alkyl chain length, where optimal activity has been reported for Gram-negative bacteria with chain lengths of 14–16 alkyls.²⁴ While classic organic ILs are miscible with both water and organic solvents, recently reported POM-ILs are insoluble in water,^{9,25} allowing implementation as water purification filters, anticorrosion/antibacterial coatings for natural stones, and self-repairing acid-resistant corrosion protection.^{9,10,25,26}

POM functionalization to impart antimicrobial surface-coating properties, although less investigated, has also been exploited to modify POM and POM-IL properties. Ma et al.²⁷ demonstrated that the introduction of organoantimony groups into heteropolytungstate moieties exhibited an antibacterial activity. In these studies, the POM served as an inorganic vehicle for the bioactive component. It was found that the biological activity of the POM varied according to the functional group attached to the antimony atom, in addition to the number of incorporated organoantimony(III) groups. Complementary studies were also recently presented by Kibler et al., where POMs were functionalized with organic ligands to tune the electrochemical behavior of POM-ILs.²⁸ These works demonstrate the potential for exploring new hybrid POM-IL materials.

Recent optimization of POM-ILs has focused on application-based metrics such as melting temperature and biocidal efficacy, mainly related to the QAC chain length. However, the fundamental understanding of POM–QAC interactions and how these affect assemblages in solids and liquids offer rich opportunity for infinite tuning of the emergent behavior of these hybrid materials. Composition–structure tuning are accessed via the size, charge, chemistry, and geometry of both the POM and QAC, in addition to the POM/QAC ratio.

Alkyltin functionalization of POMs presents a unique potential for the design of a hybrid POM-IL system. The Sn–C bond of alkyltin molecules is unusually resistant (among metal–carbon bonds) to hydrolysis, rendering it compatible with POM synthesis. Moreover, a variety of organotin materials have been shown to exhibit antiviral, antitumor, and anticancer activities.^{29–31} Finally, we expect enhanced hydrophobic interactions between the organic-functionalized POMs and the QACs, improving conformal coating and durability of antimicrobial POM-IL coatings. $[(BuSn)_3(\alpha-SiW_9O_{37})]^{7-}$ was synthesized by Pope in 1996 and isolated with Cs^+ counterions, motivated by the similar size and charge of $W\equiv O^{4+}$ and SnR^{3+} units,³² as well as the presence of an inert surface capping group. This enables the use of this cluster in an established anion exchange route that is typically used to isolate POM-ILs.^{9,10,25,26}

Here, we report the synthesis, solution and solid-state characterization, biocidal properties, and film deposition of two alkyltin hybrid POM salts, $THA_3H_4[(BuSn)_3(\alpha-SiW_9O_{37})]$ ($THA\text{-}BuSn_3W_9$) and $THTDA_3H_4[(BuSn)_3(\alpha-SiW_9O_{37})]$ ($THTDA\text{-}BuSn_3W_9$), and two inorganic POM-ILs, $THA_5H_2[\alpha-PW_{11}O_{39}]$ ($THA\text{-}W_{11}$) and $THTDA_6H[\alpha-PW_{11}O_{39}]$ ($THTDA\text{-}W_{11}$) (Figure 1, THA = tetraheptylam-

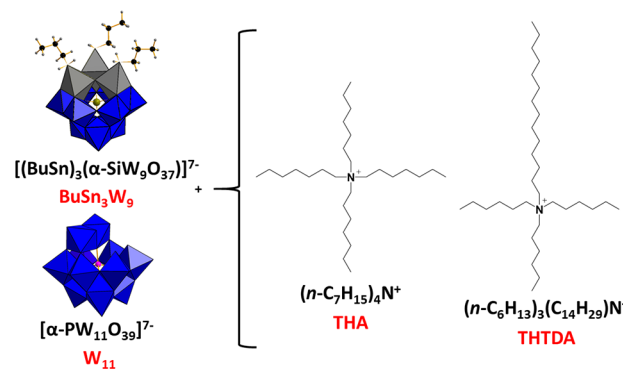


Figure 1. Cations and anions used to prepare $THA\text{-}BuSn_3W_9$, $THTDA\text{-}BuSn_3W_9$, $THA\text{-}W_{11}$, and $THTDA\text{-}W_{11}$.

monium; THTDA = tris-hexyltetradecylammonium). Our initial strategy for the choice of the inorganic POM $[\alpha-PW_{11}O_{39}]^{7-}$ was because we presumed it to have the same charge as $[(BuSn)_3(\alpha-SiW_9O_{37})]^{7-}$ with the same number of charge-balancing QACs, which influences the structure and physical properties of the conformal coating. However, synthesis and characterization of the corresponding hybrid POM salts proved that we do not have precise control over the protonation of the POMs, neither the inorganic POM-ILs nor the butyltin-functionalized POM salts. Each analogue was isolated with fewer than seven QACs per POM because of the propensity for POMs to protonate. In addition, the X-ray crystal structure of $Cs_4[H_3(BuSn)_3(\alpha-SiW_9O_{37})]\cdot H_2O$ (reported here, not obtained prior by Pope³² revealed there are three protons associated with the BuSn moieties, which apparently are robustly bound to this POM).

Intriguingly, we found that in our laboratory, the reported literature syntheses produce POM-ILs with considerable salt impurities that lower the melting temperature of the POM-IL. While the inclusion of salt impurities provides a different parameter to tune physical properties, they hinder the fundamental understanding of POM-ILs. Therefore, we present a modified synthesis that requires multiple extraction/ion-exchange steps of the POM into the organic media. Nonetheless, the influence of the butyltin group on the physical properties of the hybrid POM salt became apparent in this study. In particular, the QAC- W_{11} as surface coatings have poor adhesion, while the QAC- $[(BuSn)_3(\alpha-SiW_9O_{37})]$ show excellent adhesion and durability. We attribute this to the hydrophobic interactions between the butyltin groups and the QACs. All the synthesized hybrid POM salts show similar, potent biocidal behavior (*Escherichia coli* (*E. coli*)).

EXPERIMENTAL SECTION

Materials and Methods. $K_7[\alpha-PW_{11}O_{39}] \cdot xH_2O$ (KPW_{11}) and $Cs_4H_3[(BuSn)_3(\alpha-SiW_9O_{37})] \cdot xH_2O$ ($CsBuSnW_9$) were prepared according to published procedures and isolated as microcrystalline white powders.^{32,33} For structural determination, $CsBuSnW_9$ was recrystallized from hot water. Tetraheptylammonium bromide and trihexyltetradecylammonium bromide (as well as all solvents) were purchased from Sigma-Aldrich and used as received.

Synthesis of Hybrid POM Salts. $CsBuSnW_9$ was dissolved in 17 mL of DI water, reactant equivalents, as shown in Table 1. Stoichiometric amounts of QBr were then dissolved in toluene. The two phases were combined and mixed thoroughly. The organic phase was extracted using a separatory funnel. The aqueous solutions of the POM were reintroduced to the same organic phase for a total of four

Table 1. Summary of Hybrid POM Reactant Equivalents and Yield

	alkali-POM (mmol)	equiv (Q)Br (mmol)	yield % (based on POM)
THA-BuSn ₃ W ₉	0.26	1.8	71
THTDA-BuSn ₃ W ₉	0.26	1.8	92
THA-W ₁₁	0.26	1.8	46
THTDA-W ₁₁	0.26	1.8	50

extractions. The final organic phase product was rotovapped under reduced pressure to isolate the final viscous/waxy product.

Characterization Techniques. Single-Crystal X-ray Diffraction. Single crystals of CsBuSnW₉ were grown by dissolving 100 mg of CsBuSnW₉ in 500 μ L at 80 °C in a 4 dram vial. After complete dissolution, the vial was capped and left to slowly cool. After 3 days, single crystals of CsBuSnW₉ appeared. CsBuSnW₉ (CSD 2055317) was collected on a Rigaku Oxford Synergy-S equipped with a PhotonJet-S Cu source ($\lambda = 1.54178 \text{ \AA}$) and hyPix-6000HE photon counting detector. All images were collected and processed using CrysAlis^{Pro} Version 171.40_64.53 (Rigaku Oxford Diffraction, 2018).³⁴ After integration, both analytical absorption and empirical absorption (spherical harmonic, image scaling, detector scaling) corrections were applied.³⁵ The structure was solved by the Intrinsic Phasing method from the SHELXT program,³⁶ developed by successive difference Fourier syntheses, and refined by full-matrix least square on all F^2 data using SHELX³⁷ via the OLEX2 interface.³⁸ Crystallographic information for the structure reported can be obtained free of charge from the Cambridge Crystallographic Data Center (<https://www.ccdc.cam.ac.uk/>) upon referencing CSD number 2055317.

Notes on Refinement. Several A-level alerts result from the strong absorption of the crystal. Empirical absorption correction was applied before frame scaling. Several other methods were tried before ultimately using analytical absorption resulting R_{int} after an absorption correction of 9.81% (from 11.22%).³⁹ Nevertheless, large residual electron density less than 1 \AA away from the W and Cs atoms remained. No hydrogen atoms were directly observed for the butyl ligands, the lattice water, nor the protons bound to the cluster. Crystallographic information and additional structural information are provided in Table S1.

Small Angle X-ray Scattering. X-ray scattering data were collected on an Anton Paar SAXSess instrument using Cu K α radiation (1.54 \AA) and line collimation. The instrument was equipped with a 2D image plate for data collection in the $q = 0.018\text{--}2.5 \text{ \AA}^{-1}$ range. The lower q resolution is limited by the primary beam. Approximately 3–4 mmol solutions were measured in 1.5 mm glass capillaries (Hampton Research). The scattering data of neat solvent were collected for background subtraction. Scattering was measured for 30 min for every experiment. We used SAXSQUANT software for data collection and treatment (normalization, primary beam removal, background subtraction, desmearing, and smoothing to remove the extra noise created by the desmearing routine). All analyses and curve fitting to determine R_g , size, shape, and size distribution were carried out utilizing IRENA⁴⁰ macros with the IgorPro 6.3 (Wavemetrics) software. To simulate scattering data from the crystal structure, we used SolIX software.⁴¹

NMR. ¹H, proton-decoupled ¹³C, and proton-decoupled ¹¹⁹Sn NMR were acquired on a Bruker AV-III HD with a Prodigy cryoprobe (600.130 MHz for ¹H, 150.903 MHz for ¹³C, and 223.792 MHz for ¹¹⁹Sn) at 25.0 °C. Proton-decoupled ³¹P NMR were collected on a 400 MHz Bruker UltraShield Plus spectrometer (161.976 MHz for ³¹P). Chemical shifts are reported in parts per million (δ) and are referenced to external standards tetramethylsilane (for ¹H), tin tetrachloride (for ¹¹⁹Sn), and 85% H₃PO₄ in H₂O (for ³¹P).

Electrospray Ionization Mass Spectrometry. Electrospray ionization mass spectrometry (ESI-MS) was carried out using an Agilent 6230 ESI-MS system comprising a time-of-flight mass spectrometer coupled to an electrospray ionizer. THA₃H₄[BuSn]₃(α -SiW₉O₃₇)]

and THTDA₃H₄[BuSn]₃(α -SiW₉O₃₇)] (both 1 mM) were dissolved in a 50/50 methanol/toluene mixture. THA₃H₂[α -PW₁₁O₃₉] and THTDA₆H[α -PW₁₁O₃₉] (both 1 mM) were dissolved in a 50/50 methanol/chloroform mixture. All solutions were infused into the ESI-MS system at a flow rate of 0.4 mL min⁻¹ using a syringe pump. The solutions were nebulized with the aid of heated N₂ (325 °C) flowing at 8 L min⁻¹ and a pressure of 35 psig (241 kPa). The voltages of the capillary, skimmer, and RT octopole were set at 3500, 65, and 750 V, respectively, while the voltage of the fragmenter was set at 100 V. The data were collected in both the positive and negative ionization modes. Only the negative ionization mode showed isotopic peak envelopes for all samples.

Fourier Transform Infrared. Fourier transform infrared (FTIR) spectra were recorded on a Nicolet iS10 FTIR spectrometer with a secondary Nicolet iZ 10 module purchased from Thermo Fisher Scientific, Inc. The instrument was equipped with a diamond plate for attenuated total reflectance measurements. Spectra were collected in air for all samples.

Thermogravimetric Analysis. Thermogravimetric analysis (TGA) was performed on TA Instruments SDT Q600. Approximately 10 mg of the sample was placed in alumina crucibles for thermogravimetric measurements up to 900 °C under airflow at a heating rate of 10 °C min⁻¹.

Differential Scanning Calorimetry. Differential scanning calorimetry (DSC) was performed on TA Instruments SDT Q600. Approximately 10 mg of the sample was placed in alumina crucibles for measurements under airflow at a heating and cooling rate of 2 °C min⁻¹. Measurement parameters were dependent upon the melting points of the hybrid POM salts.

Scanning Electron Microscopy and Energy-Dispersive X-ray Spectroscopy. Scanning electron microscopy (SEM) and energy-dispersive X-ray spectroscopy (EDX) measurements were performed on a Quanta 600 SEM to extract the compositional information of all the samples.

Film Preparation for AFM Analyses. All samples were prepared by drop-casting a very small (1–2 mm diam) drop of $\sim 3 \times 10^{-3}$ M solutions of the hybrid POM salts in 50/50 THF and toluene onto a p-doped, 200 nm Si(100) wafer. The oxide surfaces were rinsed with water and dried before deposition. Great wettability was observed. Sample deposition occurred by depositing enough hybrid POM solution to uniformly cover the 1 × 1 in. wafer, spin coating at 2000 rpm for 15 s, and a postapplication bake at 185 °C for 3 min.

Atomic Force Microscopy of Films. Atomic force microscopy (AFM) images were collected on a Bruker Veeco Innova scanning probe microscope operating in the tapping mode. The tip was an aluminum sharp RTESPA probe with 40 N/m spring constant, 300 kHz resonant frequency, and 8–12 nm radius of curvature. Scanning was done for 5 × 5 μm^2 collection areas with a typical rate of 1 Hz and 256 lines. Image processing was performed using Gwyddion⁴² for leveling, background subtraction, coloring, and noise removal.

Ellipsometry of Films. The data were collected on a JA Woollam M-2000 ellipsometer over the interval of 400–1000 nm and modeled using the Cauchy equation. Thickness and refractive index (n) were measured, and the mean square error was used to determine goodness of fit.

Growth of *E. coli* Exposed to Hybrid POM Salts/DMSO. The growth of *E. coli* in the presence of various concentrations of THA₃H₄[BuSn]₃(α -SiW₉O₃₇]), THTDA₃H₄[BuSn]₃(α -SiW₉O₃₇]), THA₃H₂[α -PW₁₁O₃₉], and THTDA₆H[α -PW₁₁O₃₉] was measured to investigate the biocidal nature of the various materials. Laboratory cultures of *E. coli* were grown at 37 °C in sterile LB media composed of 5 g tryptone, 2.5 g yeast extract, and 5 g sodium chloride for 24–48 h prior to experimentation. Each test material was diluted from the initial stock concentrations in DMSO to twice the final concentrations required for exposure with LB media (while holding DMSO concentration constant), and 100 μL of each concentration was added to three replicate wells of a 96-well plate. Control wells with only LB media and DMSO were also prepared such that the final exposure concentrations were 0 (control), 0.0005, 0.001, 0.005, 0.01, 0.05, and 0.1 mg/mL.

Bulk *E. coli* culture was diluted with LB media to achieve an initial cell count of 1,000,000 cells/mL, and 100 μ L of the diluted *E. coli* culture was also added to each well of the 96-well plate to achieve a final initial cell count of 500,000 cells/mL. The plate was covered and incubated for 24 h at 37 °C. After incubation, 1 μ L of SYTOX Green Dead Cell Stain (Life Technologies Co., Eugene, OR, USA) was added to each well and the plate was covered and incubated in the dark for 20 min. Following the dark incubation with the stain, total and dead cell counts for each well were determined by flow cytometry using a BD Acurri C6 Flow Cytometer (BD Biosciences, San Jose, CA, USA). Total and dead cell counts after 24 h were compared to the initial cell counts to determine the impact of the materials at each concentration on culture growth. Statistical analysis of differences between material and control growth and growth among material types at each concentration were performed as ANOVA in SigmaPlot Version 14.0 (Systat Inc., San Jose, CA).

RESULTS AND DISCUSSION

Crystallization and structure determination of $[(BuSn)_3SiW_9O_{37}]^{7-}$, fully formulated $Cs_4[H_3(BuSn)_3SiW_9O_{37}] \cdot 16H_2O$, revealed the protonated state of this organofunctionalized POM, which persists in the hybrid POM salt derivatives. It crystallizes in the *P*-1 triclinic space group; the details are summarized in Table S1. There are two crystallographically unique clusters per unit cell, and a total of eight Cs cations were found per unit cell, clearly suggesting that the heptavalent cluster is tri-protonated (discussed later). The butyltin-substituted Keggin cluster has a typical A- α -Keggin tri-lacunary structure, meaning the three substituted BuSn units are corner-sharing (Figure 2). The SiO_4

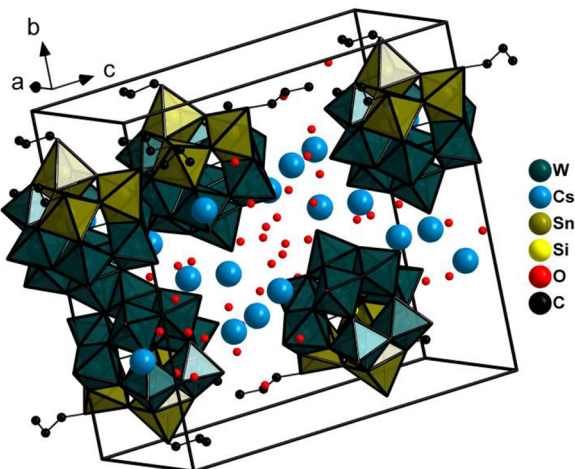


Figure 2. Unit cell view of $Cs_4[H_3(BuSn)_3SiW_9O_{37}] \cdot 16H_2O$.

central units are only slightly distorted, $Si-O \sim 1.63-1.65 \text{ \AA}$. Terminal, bridging, and central $W-O$ bond lengths are, respectively, 1.70–1.73, 1.84–1.97, and 2.35–2.42 \AA . The $Sn-C$ bonds are 2.13–2.15 \AA . All carbons of the six butyl chains (three chains per crystallography distinct POM) were located, exhibiting some disorder for carbons in the second through

fourth position for one-third of these chains (where the first carbon is bonded to Sn). The $Sn-O$ bonds that bridge to W are 2.04–2.07 \AA , while those that bridge to neighboring Sn in the corner-linked Sn_3 trimer are distinctly longer, 2.07–2.12 \AA . Bond valence sum (BVS) calculations located the three protons per cluster on the $Sn-O_b-Sn$ bridging oxygen (BVS on O_b range from 1.1 to 1.3; Table S2 and Figure S1).

All hybrid POM salts were synthesized, as described in the literature,^{9,10,25,26} except that our syntheses necessitated four iterative extractions into toluene for all POM salt combinations, using seven equivalents of the QAC for each extraction. In addition, fresh, aqueous solutions of $CsBuSnW_9$ were implemented in each individual extraction (synthetic conditions, Experimental Section). All literature procedures report a single extraction process followed by a solvent stripping step. We found that four subsequent extractions were necessary to get rid of excess Br^- in the hybrid POM salts isolated from organic media, as shown in Tables S3–S10 and Figures S2–S5. The ion-exchange products with excess Br^- , ~20% to 64%, were viscous liquids, whereas the bromine-free hybrid POM salts from multiple ion exchanges are solids at room temperature. Table S9 shows that one extraction step is not enough to completely exchange all ions, as shown by the potassium content (~10 wt %). Overall, the EDX data for the multiple ion-exchange products showed both low bromide and alkali impurities (<2%). This allows the characterization of the physical properties of these materials without starting material impurities. In summary, while bromide impurities yield better metrics for ionic liquids (lower melting temperature), they do not reflect the true characteristics of the hybrid POM salt, which can be robustly reproduced. The observed lower melting temperatures may simply be based on the higher organic (QAC) content.

All FTIR spectra (Figures S6–S9) exhibit characteristic absorptions because of C–H stretching and bending ~3000 cm^{-1} (stretch), ~1470 cm^{-1} (scissor), and 1370 cm^{-1} (methyl rock) from both the butyl ligands and alkylammonium ions. The C–C stretch was also presented in all spectra at ~1100 cm^{-1} , as well as broad $W-O$ vibrational stretches below 1000 cm^{-1} , characteristic of polyoxotungstates. POM/QAC ratios were determined from TGA curves, quantifying the loss of organic counterions and butyl ligands. The TGA curves in Figures S10–S13 show that alkylammonium ions start to decompose and evaporate at ~210 °C and that there are higher ratios of THTDA/PW₁₁ than THA/PW₁₁, where incomplete exchange is balanced by H⁺ counterions. Table 2 summarizes the formulae for the four POM derivatives, determined by thermogravimetry. The DSC curves (Figures S14–S17) show melting temperatures of ~26 °C (THTDA-W₁₁), ~60 °C (THA-W₁₁), ~105 °C (THTDA-BuSn₃W₉), and ~132 °C (THA-BuSn₃W₉), as summarized in Table 2. The corresponding melting temperatures were also verified by a capillary melting point apparatus. A possible glass transition is only observed for the highest melting temperature

Table 2. Formula, Weight Loss, and Melting Temperatures for the Four Hybrid POM Salts, Determined by TGA

	weight loss (%)	formula	MP (°C)
THA-BuSn ₃ W ₉	~41	$THA_3H_4[(BuSn)_3(\alpha-SiW_9O_{37})]$	~132
THTDA-BuSn ₃ W ₉	~44	$THTDA_3H_4[(BuSn)_3(\alpha-SiW_9O_{37})]$	~105
THA-W ₁₁	~45	$THA_3H_2[\alpha-PW_{11}O_{39}]$	~60
THTDA-W ₁₁	~51	$THTDA_6H[\alpha-PW_{11}O_{39}]$	~26

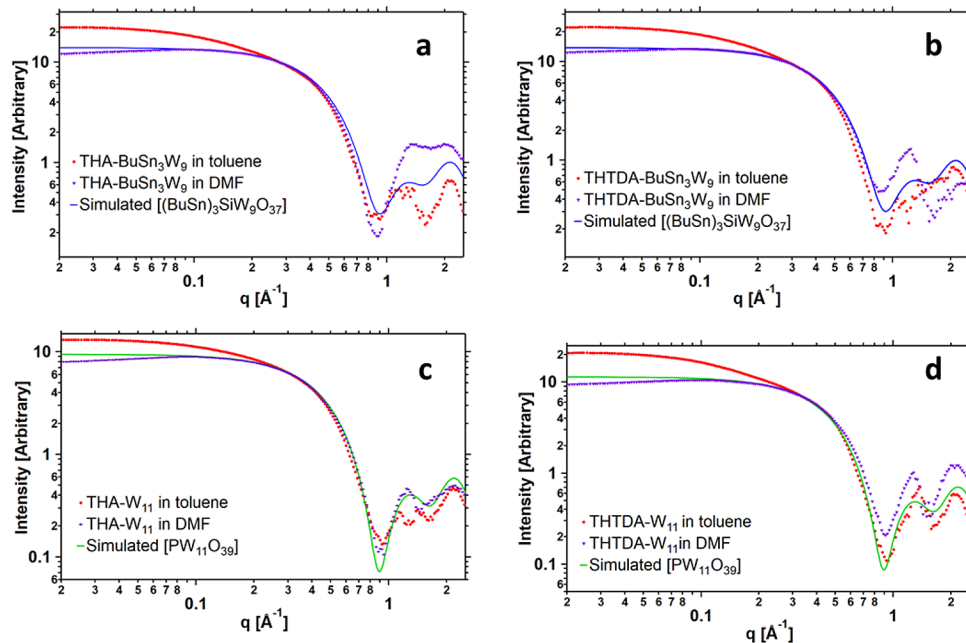


Figure 3. SAXS of $\text{THA}_3\text{H}_4[(\text{BuSn})_3(\alpha\text{-SiW}_9\text{O}_{37})]$, $\text{THTDA}_3\text{H}_4[(\text{BuSn})_3(\alpha\text{-SiW}_9\text{O}_{37})]$, $\text{THA}_5\text{H}_2[\alpha\text{-PW}_{11}\text{O}_{39}]$, and $\text{THTDA}_6\text{H}[\alpha\text{-PW}_{11}\text{O}_{39}]$, 20 mg/mL, in toluene and DMF.

hybrid POM salt ($\text{THA}\text{-BuSn}_3\text{W}_9$) at 80 °C (Figure S14). Glass transition was not observed in any of the DSC curves; it is possible that they are below room temperature, where previous POM-ILs were reported.^{9,43} Figure S18a–d shows two cycles of heating and cooling. The melting temperature peak is only observable in the first cycle for THTDA-W_{11} and THA-W_{11} but is observable for both cycles for $\text{THTDA-BuSn}_3\text{W}_9$ and $\text{THA-BuSn}_3\text{W}_9$. For the PW_{11} analogues, we assume that in the second cycle, remelting likely occurs over a broader temperature range; therefore, a distinct peak is not so apparent. We tentatively suggest that interactions between ions are stronger and more selective in the BuSn_3W_9 compounds, yielding a more distinct melting temperature, visible in the second cycle. Thin film properties discussed later supports this conclusion.

In general, longer-chain QACs and higher QAC/POM ratios yielded lower melting temperatures. Even though $\text{THA}/\text{THTDA-BuSn}_3\text{W}_9$ species appear to be nonconventional ILs, meaning their melting points are above 100 °C, butyltin functionalization does decrease the melting points in comparison with the parent Keggin ion $\text{THA}_4[\alpha\text{-SiW}_{12}\text{O}_{40}]$ (mp ~170 °C).⁹ The lower melting temperatures of the THTDA derivatives are attributed to both the higher organic content in these hybrid POM salts and the asymmetry derived from the single longer chain, decreasing the order of these assemblies. Finally, we can tentatively say that the butyl chains of BuSn_3W_9 can interact with the QAC alkyl chains, increasing the melting temperature relative to that of the $[\alpha\text{-PW}_{11}\text{O}_{39}]^{7-}$ derivatives.

X-ray Scattering. SAXS is useful for describing dynamic solution behavior based on interactions between ions in solution, leading to behavior during the deposition of coatings or thin films. $\text{THA-BuSn}_3\text{W}_9$, $\text{THTDA-BuSn}_3\text{W}_9$, THA-W_{11} , and THTDA-W_{11} are completely insoluble in water, affirming their hydrophobic nature. A variety of nonpolar and polar organic solvents were utilized to study their solution behavior. Figure 3 presents the simulated and experimental SAXS data

for $\text{THA-BuSn}_3\text{W}_9$ (a), $\text{THTDA-BuSn}_3\text{W}_9$ (b), THA-W_{11} (c), and THTDA-W_{11} (d). In DMF, $\text{THA-BuSn}_3\text{W}_9$ and $\text{THTDA-BuSn}_3\text{W}_9$ appear pure and monodisperse, with no evidence for interactions between POMs and/or QACs in solution. There is a good agreement between the experimental and simulated scattering curves in the Guinier region ($q \sim 0.4 \text{ \AA}^{-1}$). The slight deviation of the experimental scattering (below $q = 0.07 \text{ \AA}^{-1}$ in each) suggests some ordering of the POMs in solution, because of the charge repulsion between POM anions. In contrast, in toluene, there is evidence for larger aggregates for both the THA and THTDA hybrid POM salts. This is observed by the shift in the Guinier region (between $q = 0.4$ and 0.9 \AA^{-1}). A two-phase fit of the SAXS data shows that only ~2% of the total POM population is aggregated into a ~30 Å diameter agglomerates, compared to the 10 Å diameter of the Keggin ion POM (Table S11; Figures S19 and S20). A very similar behavior is observed for THA-W_{11} and THTDA-W_{11} in both toluene and DMF (Table S11; Figures S21 and S22), suggesting that the behavior is unrelated to the butyltin group. Notably, although only a small percent of the POMs is aggregated in toluene, the scattering initial scattering intensity (I_0) approximately doubles. This is because the intensity is proportional to (particle volume)³. The aggregates likely are composed mainly of the POMs rather than a mixture of POMs plus QACs because the scattering intensity also has a z^2 dependence (z = atomic number). Since the aggregation is not specific to the BuSn_3W_9 , the W_{11} , or either of the QACs, we envision aggregates of POMs (~5 to 8) in inverse micelles created by the QACs. The POM–POM association can be via hydrophobic interactions of the butyl chains of BuSn_3W_9 or H bonding of protonated POMs. In summary, the polar DMF produces solutions of well-separated POMs and counterions, while nonpolar toluene promotes some inverse micelle formation of POMs surrounded by QACs. This differing solvent-dependent behaviors can affect association during deposition of coatings.

Tin and Phosphorus NMR. ^{119}Sn NMR of THA-BuSn₃W₉ and THTDA-BuSn₃W₉ in benzene (100% C₆D₆) and THF/10% DMSO-d₆ shows the tri-substituted Keggin clusters predominantly as the α -isomer with a minor β -isomer component.³² The peaks are located at approximately -500 ppm, as shown in Figure 4, consistent with six-coordinate tin.³²

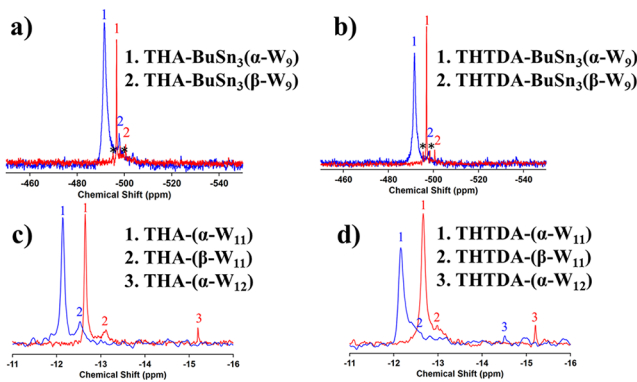


Figure 4. (a,b) ^{119}Sn NMR of $\text{THA}_3\text{H}_4[(\text{BuSn})_3(\alpha\text{-SiW}_9\text{O}_{37})]$ and $\text{THTDA}_3\text{H}_4[(\text{BuSn})_3(\alpha\text{-SiW}_9\text{O}_{37})]$ in 100% C₆D₆ (blue) and THF/10% dimethylsulfoxide-d₆ (red). (c,d) ^{31}P NMR of $\text{THA}_5\text{H}_2[\alpha\text{-PW}_{11}\text{O}_{39}]$ and $\text{THTDA}_6\text{H}[\alpha\text{-PW}_{11}\text{O}_{39}]$ in toluene/10% dimethylsulfoxide-d₆ (blue) and 100% CDCl₃ (red). * denotes ^{117}Sn satellites.

In the more polar THF/10% DMSO-d₆ solvent, the peaks are sharp and ^{117}Sn satellites are apparent with $J(^{117}\text{Sn}^{119}\text{Sn}) \sim 550$ Hz. In benzene (100% C₆D₆), peak broadening suggests some anisotropic behavior. This is consistent with the SAXS data, where we observe some aggregation in nonpolar solvents (benzene (100% C₆D₆) and toluene), and well-separated clusters in polar solvents (THF/10% DMSO-d₆ and DMF). ^{31}P NMR of THA-W₁₁ and THTDA-W₁₁ (chloroform (100% CDCl₃) and toluene/10% DMSO-d₆) exhibited one dominant peak approximately from -12 to -13 ppm (Figure 4) consistent with tetrahedral phosphorus in $[\alpha$ -

$\text{PW}_{11}\text{O}_{39}]^{7-}$.^{28,44-46} These are also consistent with the SAXS data, showing more broadening in nonpolar toluene/10% DMSO-d₆ than in polar chloroform (100% CDCl₃). Proton and carbon NMR were also performed (Figures S23–S27 and S29–S32) but are not discussed here because of the lack of added information.

Mass Spectrometry. Both tin and tungsten have multiple natural isotopes, yielding characteristic peak envelopes leading to very precise assignments (Figures 5 and S33–S37; Table 3). These characterizations confirm the predominance of the targeted Keggin synthons. THTDA-BuSn₃W₉ also contain minor alkali metal impurities that become evident in ESI-MS analysis, but SEM-EDX (Table S6) confirmed that the overall alkali metal content is negligible. THA-W₁₁ and THTDA-W₁₁ ionized primarily as alkylammonium PW₁₁ and PW₁₀ species in chloroform/methanol mixtures. PW₁₀ species contained some potassium impurities from the starting material, which is not surprising given its propensity to sit in the lacunary hole. Again, these impurities are minor, based on compositional analyses.

Antimicrobial Activity. The antimicrobial activity of all hybrid POM salts toward Gram-negative bacteria, *E.coli*, was investigated by measuring the impacts of the materials on *E.coli* cell growth across a range of concentrations. Although the materials had no significant impacts on the number of live cells, there was a significant increase in the dead cell population over 24 h that increased for all hybrid POM salts with increasing POM concentration compared to control treatments (Figure 6). The percent increase for total *E. coli* dead cell count over all hybrid POM salt types and concentrations ranged from 5.8% to 35.5% of the control dead cell count. THA-W₁₁ and THTDA-BuSn₃W₉ had the lowest concentrations at which significant increases in the number of dead cells were present in the culture at 0.0005 mg/mL, meaning that they had the highest efficacy against *E. coli*, followed by THTDA-W₁₁ at 0.001 mg/mL, and finally, THA-BuSn₃W₉, at 0.01 mg/mL. Although butyltin functionalization led to significantly lower

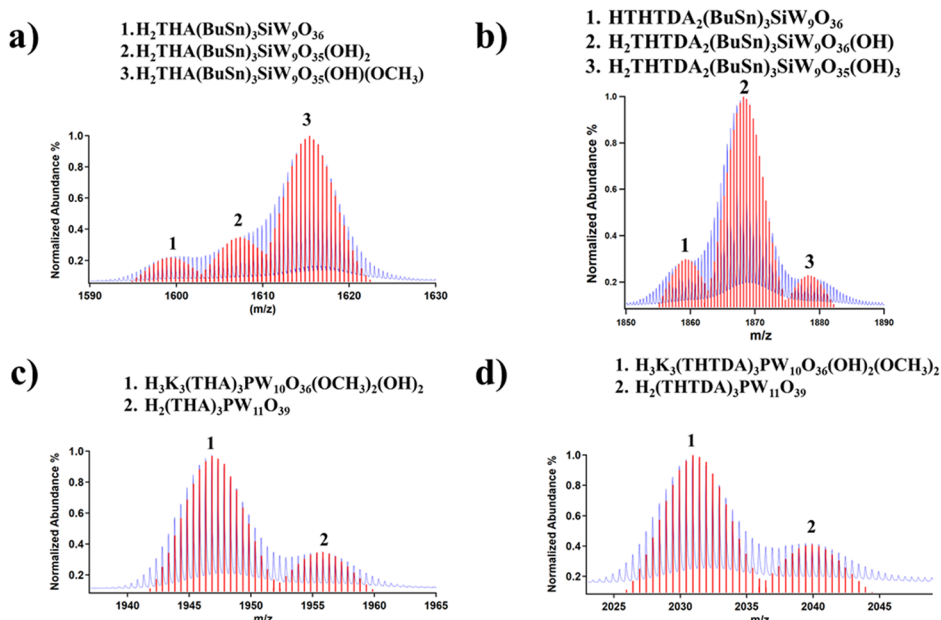


Figure 5. ESI-MS, negative mode (100V), of $\text{THA}_3\text{H}_4[(\text{BuSn})_3(\alpha\text{-SiW}_9\text{O}_{37})]$ (a), $\text{THTDA}_3\text{H}_4[(\text{BuSn})_3(\alpha\text{-SiW}_9\text{O}_{37})]$ (b), $\text{THA}_5\text{H}_2[\alpha\text{-PW}_{11}\text{O}_{39}]$ (c), and $\text{THTDA}_6\text{H}[\alpha\text{-PW}_{11}\text{O}_{39}]$ (d) in 50/50 toluene/MeOH (a,b) and 50/50 chloroform/MeOH (c,d).

Table 3. $\text{THA}_3\text{H}_4[(\text{BuSn})_3(\alpha\text{-SiW}_9\text{O}_{37})]$, $\text{Cs}/\text{Na}/\text{THTDA}_3\text{H}_4[(\text{BuSn})_3(\alpha\text{-SiW}_9\text{O}_{37})]$, $\text{THA}_5\text{H}_2[\alpha\text{-PW}_{11}\text{O}_{39}]$, and $\text{THTDA}_6\text{H}[\alpha\text{-PW}_{11}\text{O}_{39}]$ Derivatives Identified in the ESI-MS^a

ion species	formula	<i>m/z</i> (obs.)	<i>m/z</i> (calc.)	rel. intensity
THA-BuSn ₃ W ₉				
M^{-2}	$\text{H}_2\text{C}_{28}\text{H}_{60}\text{N}(\text{BuSn})_3\text{SiW}_9\text{O}_{36}$	1599.381	1599.381	<20%
$(\text{M}-\text{H})^{-2}$	$\text{H}_2\text{C}_{28}\text{H}_{60}\text{N}(\text{BuSn})_3\text{SiW}_9\text{O}_{35}(\text{OH})_2$	1608.388	1608.387	~30%
M^{-2}	$\text{H}_2\text{C}_{28}\text{H}_{60}\text{N}(\text{BuSn})_3\text{SiW}_9\text{O}_{35}(\text{OH})(\text{OCH}_3)$	1615.393	1615.395	100%
M^{-2}	$\text{C}_{56}\text{H}_{120}\text{N}_2(\text{BuSn})_3\text{SiW}_9\text{O}_{35}(\text{OH})$	1804.115	1804.114	<10%
M^{-2}	$\text{HC}_{56}\text{H}_{120}\text{N}_2(\text{BuSn})_3\text{SiW}_9\text{O}_{35}(\text{OH})_2$	1813.119	1813.119	~60%
M^{-2}	$\text{NaHC}_{56}\text{H}_{120}\text{N}_2(\text{BuSn})_3\text{SiW}_9\text{O}_{35}(\text{OH})_2$	1824.604	1824.614	<10%
THTDA-BuSn ₃ W ₉				
M^{-2}	$\text{Cs}_2\text{NaH}(\text{BuSn})_3\text{SiW}_9\text{O}_{31}(\text{OCH}_3)_5(\text{OH})_6$	1626.609	1626.608	~40%
$(\text{M}-\text{H})^{-2}$	$\text{Cs}_2\text{NaH}(\text{BuSn})_3\text{SiW}_9\text{O}_{31}(\text{OCH}_3)_5(\text{OH})_5$	1632.607	1632.608	~35%
M^{-2}	$\text{Cs}_2\text{Na}_2\text{H}(\text{BuSn})_3\text{SiW}_9\text{O}_{33}(\text{OCH}_3)_6(\text{OH})_2$	1635.607	1635.602	~45%
$(\text{M}-\text{H})^{-2}$	$\text{Cs}_2\text{NaH}(\text{BuSn})_3\text{SiW}_9\text{O}_{31}(\text{OCH}_3)_7(\text{OH})_4$	1639.608	1639.616	~40%
M^{-2}	$\text{Cs}_2\text{Na}_2\text{H}(\text{BuSn})_3\text{SiW}_9\text{O}_{33}(\text{OCH}_3)_7(\text{OH})$	1642.608	1642.610	~50%
$(\text{M}-\text{H})^{-2}$	$\text{HC}_{64}\text{H}_{136}\text{N}_2(\text{BuSn})_3\text{SiW}_9\text{O}_{36}$	1859.186	1859.169	~20%
$(\text{M}-\text{H})^{-2}$	$\text{H}_2\text{C}_{64}\text{H}_{136}\text{N}_2(\text{BuSn})_3\text{SiW}_9\text{O}_{36}(\text{OH})$	1868.184	1868.174	100%
M^{-2}	$\text{H}_2\text{C}_{64}\text{H}_{136}\text{N}_2(\text{BuSn})_3\text{SiW}_9\text{O}_{35}(\text{OH})_3$	1878.163	1878.187	~20%
THA-W ₁₁				
M^{-3}	$\text{N}_2\text{C}_{56}\text{H}_{120}\text{PW}_{11}\text{O}_{38}$	1161.058	1161.064	~40%
M^{-2}	$\text{H}_3\text{K}_3\text{N}_3\text{C}_{84}\text{H}_{180}\text{PW}_{10}\text{O}_{36}(\text{OCH}_3)_2(\text{OH})_2$	1946.827	1946.840	100%
M^{-2}	$\text{H}_2\text{N}_3\text{C}_{84}\text{H}_{180}\text{PW}_{11}\text{O}_{39}$	1955.833	1955.838	~30%
THTDA-W ₁₁				
M^{-3}	$\text{H}_3\text{K}_3\text{N}_2\text{C}_{64}\text{H}_{136}\text{PW}_{10}\text{O}_{36}(\text{OH})_2(\text{OCH}_3)_2$	1198.432	1198.444	~78%
M^{-2}	$\text{H}_4\text{K}_3\text{N}_2\text{C}_{64}\text{H}_{136}\text{PW}_{10}\text{O}_{36}(\text{OH})_2(\text{OCH}_3)_2$	1798.167	1798.170	~5%
M^{-2}	$\text{H}_3\text{N}_2\text{C}_{64}\text{H}_{136}\text{PW}_{11}\text{O}_{39}$	1807.161	1807.168	~20%
M^{-2}	$\text{H}_3\text{K}_3\text{N}_3\text{C}_{96}\text{H}_{204}\text{PW}_{10}\text{O}_{36}(\text{OH})_2(\text{OCH}_3)_2$	2030.921	2030.934	100%
M^{-2}	$\text{H}_2\text{N}_3\text{C}_{96}\text{H}_{204}\text{PW}_{11}\text{O}_{39}$	2039.923	2039.932	~22%

^aNegative mode, 100 V. Generally species below 15% were not assigned.

E. coli Inhibition Percentage as POM Concentration Increases

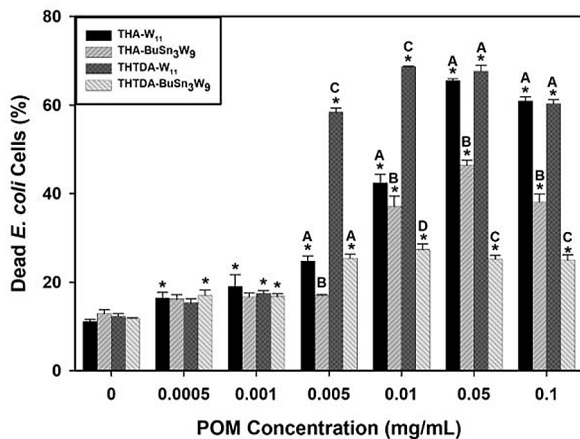


Figure 6. *E. coli* inhibition % of $\text{THA}_3\text{H}_4[(\text{BuSn})_3(\alpha\text{-SiW}_9\text{O}_{37})]$, $\text{THTDA}_3\text{H}_4[(\text{BuSn})_3(\alpha\text{-SiW}_9\text{O}_{37})]$, $\text{THA}_5\text{H}_2[\alpha\text{-PW}_{11}\text{O}_{39}]$, and $\text{THTDA}_6\text{H}[\alpha\text{-PW}_{11}\text{O}_{39}]$ at a variety of concentrations (mg/mL) measured over 24 h. Asterisk (*) represents significant difference ($p \leq 0.05$) compared to control populations without any POMs. Uppercase letters (A, B, C, and D) represent significant differences among the hybrid POM salts within a given exposure concentration.

dead cell counts in comparison with the lacunary derivatives at POM concentrations >0.005 mg/mL, they still had a significant biocidal activity. We hypothesize that the biocidal nature is primarily a function of the QAC counterions, since we experimentally observed higher ratios of THA/

THTDA:PW₁₁ by TGA (Table 2) compared to the butyltin derivatives.

Thin Film Deposition. The most significant effect of butyltin functionalization is observed in the behavior of hybrid POM salt coatings. All hybrid POM salts were drop casted from $\sim 3 \times 10^{-3}$ M solutions in 50/50 THF/toluene onto a p-doped, 200 nm Si(100) wafer and baked to 185 °C to ensure the removal of excess solvent. The films cast from THA-BuSn₃W₉ and THTDA-BuSn₃W₉ initially exhibited relatively smooth films by both AFM and ellipsometry measurements (RMS (sq) (nm) <1) (Table S12). To test the durability of these coatings, AFM measurements were performed again after letting the films sit in air for 3 months. Both butyltin-functionalized films exhibited similar morphologies and thicknesses before and after this time period (Figures 7 and S38): THTDA-BuSn₃W₉ films exhibited strikingly close RMS (sq) (nm) values with time, indicating minimal change (Table S12). In contrast, films cast from THA-W₁₁ and THTDA-W₁₁ did not demonstrate this behavior. THA-W₁₁ films initially exhibited smooth, conformal coatings; however, after 1 month, rougher film morphologies were observed by ellipsometry (Figure S39). This phenomenon was even more prominent with the THTDA-W₁₁ films, where increased surface roughness was observed after a single day (Figure S40). We hypothesize that the asymmetric hydrophobic (butyltin)-hydrophilic (WO_x) nature of THA/THTDA-BuSn₃W₉ species allow for cluster–ammonium interactions on the film surface. This can occur, for example, by hydrophobic interactions of butyltin groups with the QACs. Furthermore, film dissolution did not occur for any of the films after contact with water for 1 h. To assess the hydrophobicity of THA-BuSn₃W₉, THTDA-

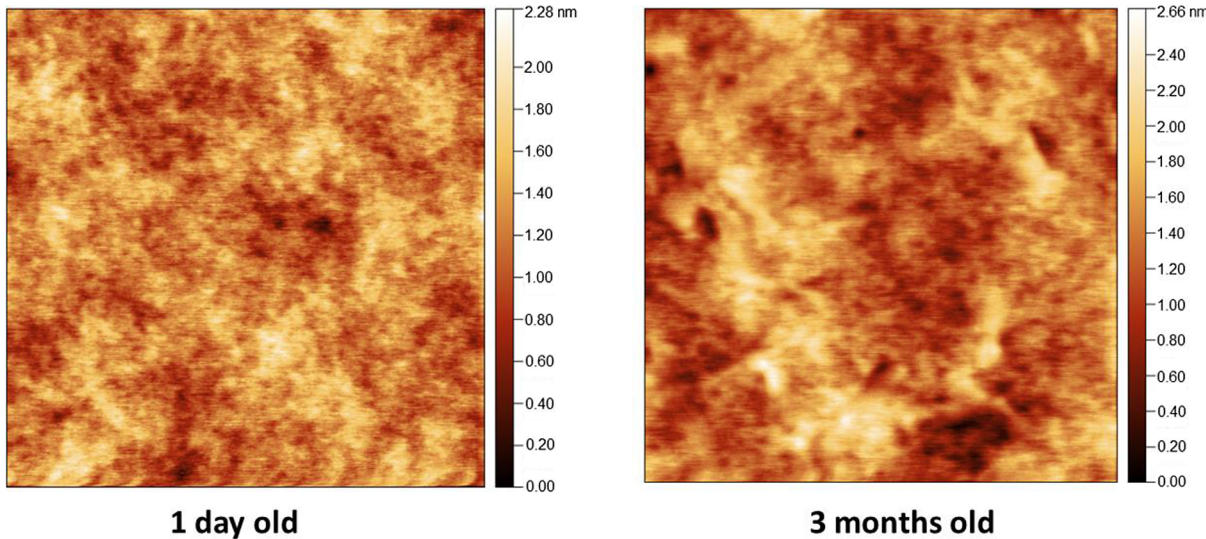


Figure 7. $1 \times 1 \mu\text{m}$ AFM image for $\sim 3 \times 10^{-3} \text{ M}$ THTDA₃H₄[$(\text{BuSn})_3(\alpha\text{-SiW}_9\text{O}_{37})$] in a 50/50 THF/toluene solution drop casted onto native oxide Si(110) with no treatment.

BuSn₃W₉, and THA-W₁₁ films, 1 μL of water was dropped onto the surface by the sessile drop method and contact angles were measured. All hybrid POM-functionalized films exhibited significantly higher contact angles compared to bare SiO₂ (Figures S41–S44), ranging from 74° to 78°. THTDA-BuSn₃W₉ exhibited a contact angle of 78.7°, significantly higher than those reported previously.^{9,10}

SUMMARY AND CONCLUSIONS

In summary, we report the synthesis, characterization, and film deposition of two new hybrid butyltin POM salts, THA₃H₄[$(\text{BuSn})_3(\alpha\text{-SiW}_9\text{O}_{37})$] and THTDA₃H₄[$(\text{BuSn})_3(\alpha\text{-SiW}_9\text{O}_{37})$], and two inorganic POM-ILs, THA₅H₂[$\alpha\text{-PW}_{11}\text{O}_{39}$] and THTDA₆H[$\alpha\text{-PW}_{11}\text{O}_{39}$], for comparison of differentiating properties engendered by the butyltin functionalization. Importantly, the purity of these compounds enables for an accurate representation of thermal properties, solution behavior, biocidal activity, and surface functionalization. In our experience and in contrast to prior reports, the complete replacement of the Br⁻ with POMs requires four repeated contact and extraction steps of the organic solution with aqueous POM solutions. However, this may be specific to the POM and sensitive to other factors including temperature, concentration, etc. The bromine of incompletely extracted POM-ILs decreases the melting point to below room temperature, likely because of the higher QAC/POM ratio, and also suggests an additional “knob” for tuning POM-IL properties. Antimicrobial studies show that all studied hybrid POM salt derivatives exhibit biocidal activity, but THA-W₁₁ and THTDA-W₁₁ exhibited the highest efficacy against *E. coli*, attributed primarily to the QAC counterions. The most significant effect of the butyltin functionalization of the POMs is observed in the ability to prepare conformal coatings. While the POM-ILs consisting of inorganic POMs (W₁₁) are nonadherent, those composed of [$(\text{BuSn})_3(\alpha\text{-SiW}_9\text{O}_{37})$] are adherent and resistant to aging in ambient conditions, likely owed to improved interactions between the inorganic and organic components. In contrast, the lower QAC may also play a role, and it is our intent to decouple these factors by studying additional POM-ILs that have the same POM and different QAC/H⁺ ratios for charge balance. In future studies, we will

also develop protocols to test the antimicrobial properties in a coating (heterogeneous) form rather than a homogeneous form. POM-ILs are infinitely tunable based on the POM, IL, POM/IL ratio, total organic content, and so on. This study demonstrates the utility of organic functionalization of the POM. In addition to the abovementioned studies, we will also focus on how the role of POM–QAC interactions can be improved to yield dense, water resistant, and robust coatings for antimicrobial surfaces.

ASSOCIATED CONTENT

Supporting Information

The Supporting Information is available free of charge at <https://pubs.acs.org/doi/10.1021/acsami.1c03269>.

Additional data and figures including crystallographic information, compositional information, FTIR spectra, differential scanning calorimetry, SAXS, NMR, ESI-MS, AFM images, ellipsometry data, and contact angle photos ([PDF](#))

AUTHOR INFORMATION

Corresponding Author

May Nyman — Department of Chemistry, Oregon State University, Corvallis, Oregon 97331, United States;
orcid.org/0000-0002-1787-0518; Email: may.nyman@oregonstate.edu

Authors

Morgan Rose Olsen — Department of Chemistry, Oregon State University, Corvallis, Oregon 97331, United States; Department of Chemistry, Reed College, Portland, Oregon 97202, United States

Ian Colliard — Department of Chemistry, Oregon State University, Corvallis, Oregon 97331, United States

Tasnim Rahman — Department of Chemistry, Oregon State University, Corvallis, Oregon 97331, United States

Taiki C. Miyaishi — Department of Environmental and Molecular Toxicology, Oregon State University, Corvallis, Oregon 97331, United States; School of Chemical, Biological

and Environmental Engineering, Oregon State University, Corvallis, Oregon 97331, United States

Bryan Harper – Department of Environmental and Molecular Toxicology, Oregon State University, Corvallis, Oregon 97331, United States

Stacey Harper – Department of Environmental and Molecular Toxicology, Oregon State University, Corvallis, Oregon 97331, United States; School of Chemical, Biological and Environmental Engineering, Oregon State University, Corvallis, Oregon 97331, United States; orcid.org/0000-0001-7043-7097

Complete contact information is available at:
<https://pubs.acs.org/10.1021/acsami.1c03269>

Notes

The authors declare no competing financial interest.

ACKNOWLEDGMENTS

The synthesis and characterization of solutions, solids, and thin films were carried out with support from the National Science Foundation (NSF; Center for Sustainable Materials Chemistry) under Grant CHE-1606982. The biocidal studies were supported by NSF CBET-1762245.

REFERENCES

- (1) Donlan, R. M. Biofilms: Microbial Lifes on Surfaces. *Emerg. Infect. Dis.* **2002**, *8*, 881–890.
- (2) Knetsch, M. L. W.; Koole, L. H. New Strategies in the Development of Antimicrobial Coatings: The Example of Increasing Usage of Silver and Silver Nanoparticles. *Polymers (Basel)* **2011**, *3*, 340–366.
- (3) Rai, A.; Prabhune, A.; Perry, C. C. Antibiotic Mediated Synthesis of Gold Nanoparticles with Potent Antimicrobial Activity and Their Application in Antimicrobial Coatings. *J. Mater. Chem.* **2010**, *20*, 6789–6798.
- (4) Nepal, D.; Balasubramanian, S.; Simonian, A. L.; Davis, V. A. Strong Antimicrobial Coatings: Single-Walled Carbon Nanotubes Armored with Biopolymers. *Nano Lett.* **2008**, *8*, 1896–1901.
- (5) Hu, R.; Li, G.; Jiang, Y.; Zhang, Y.; Zou, J. J.; Wang, L.; Zhang, X. Silver-Zwitterion Organic-Inorganic Nanocomposite with Antimicrobial and Antiadhesive Capabilities. *Langmuir* **2013**, *29*, 3773–3779.
- (6) Karbowniczek, J.; Cordero-Arias, L.; Virtanen, S.; Misra, S. K.; Valsami-Jones, E.; Tuchscherr, L.; Rutkowski, B.; Górecki, K.; Bala, P.; Czyszka-Filemonowicz, A.; Boccaccini, A. R. Electrophoretic Deposition of Organic/Inorganic Composite Coatings Containing ZnO Nanoparticles Exhibiting Antibacterial Properties. *Mater. Sci. Eng. C* **2017**, *77*, 780–789.
- (7) Ge, H.; Zhang, J.; Yuan, Y.; Liu, J.; Liu, R.; Liu, X. Preparation of Organic–Inorganic Hybrid Silica Nanoparticles with Contact Antibacterial Properties and Their Application in UV-Curable Coatings. *Prog. Org. Coatings* **2017**, *106*, 20–26.
- (8) Wu, S. L.; Liu, F.; Yang, H. C.; Darling, S. B. Recent Progress in Molecular Engineering to Tailor Organic-Inorganic Interfaces in Composite Membranes. *Mol. Syst. Des. Eng.* **2020**, *5*, 433–444.
- (9) Herrmann, S.; Kostrzewa, M.; Wierschem, A.; Streb, C. Polyoxometalate Ionic Liquids as Self-Repairing Acid-Resistant Corrosion Protection. *Angew. Chem., Int. Ed.* **2014**, *53*, 13596–13599.
- (10) Misra, A.; Franco Castillo, I.; Müller, D. P.; González, C.; Eyssautier-Chuine, S.; Ziegler, A.; De La Fuente, J. M.; Mitchell, S. G.; Streb, C. Polyoxometalate-Ionic Liquids (POM-ILs) as Anticorrosion and Antibacterial Coatings for Natural Stones. *Angew. Chem., Int. Ed.* **2018**, *57*, 14926–14931.
- (11) Liu, X.; Xie, X.; Du, Z.; Li, B.; Wu, L.; Li, W. Aqueous Self-Assembly of Arginine and K8SiW11O39: Fine-Tuning the Formation of a Coacervate Intended for Sprayable Anticorrosive Coatings. *Soft Matter* **2019**, *15*, 9178–9186.
- (12) Zhang, C.; Zhao, M.; Zou, H.; Zhang, X.; Sheng, R.; Zhang, Y.; Zhang, B.; Li, C.; Qi, Y. An Enhanced Antibacterial Nanoflowers AgPW@PDA@Nisin Constructed from Polyoxometalate and Nisin. *J. Inorg. Biochem.* **2020**, *212*, No. 111212.
- (13) Rajkowska, K.; Koziróg, A.; Otlewska, A.; Piotrowska, M.; Atrián-Blasco, E.; Franco-Castillo, I.; Mitchell, S. G. Antifungal Activity of Polyoxometalate-Ionic Liquids on Historical Brick. *Molecules* **2020**, *25*, No. 5663.
- (14) Misra, A.; Kozma, K.; Streb, C.; Nyman, M. Beyond Charge Balance: Counter-Cations in Polyoxometalate Chemistry. *Angew. Chem., Int. Ed.* **2020**, *59*, 596–612.
- (15) Li, J.; Chen, Z.; Zhou, M.; Jing, J.; Li, W.; Wang, Y.; Wu, L.; Wang, L.; Wang, Y.; Lee, M. Polyoxometalate-Driven Self-Assembly of Short Peptides into Multivalent Nanofibers with Enhanced Antibacterial Activity. *Angew. Chem., Int. Ed.* **2016**, *55*, 2592–2595.
- (16) Judd, D. A.; Nettles, J. H.; Nevins, N.; Snyder, J. P.; Liotta, D. C.; Tang, J.; Ermoliev, J.; Schinazi, R. F.; Hill, C. L. Polyoxometalate HIV-1 Protease Inhibitors. A New Mode of Protease Inhibition. *J. Am. Chem. Soc.* **2001**, *123*, 886–897.
- (17) Fu, L.; Gao, H.; Yan, M.; Li, S.; Li, X.; Dai, Z.; Liu, S. Polyoxometalate-Based Organic-Inorganic Hybrids as Antitumor Drugs. *Small* **2015**, *11*, 2938–2945.
- (18) Gao, N.; Sun, H.; Dong, K.; Ren, J.; Duan, T.; Xu, C.; Qu, X. Transition-Metal-Substituted Polyoxometalate Derivatives as Functional Anti-Amyloid Agents for Alzheimer's Disease. *Nat. Commun.* **2014**, *5*, No. 3422.
- (19) Absillis, G.; Parac-Vogt, T. N. Peptide Bond Hydrolysis Catalyzed by the Wells-Dawson Zr(α -2-P₂W₁₇O₆₁)₂ Polyoxometalate. *Inorg. Chem.* **2012**, *51*, 9902–9910.
- (20) Solé-Daura, A.; Goovaerts, V.; Stroobants, K.; Absillis, G.; Jiménez-Lozano, P.; Poblet, J. M.; Hirst, J. D.; Parac-Vogt, T. N.; Carbó, J. J. Probing Polyoxometalate–Protein Interactions Using Molecular Dynamics Simulations. *Chem. - Eur. J.* **2016**, *22*, 15280–15289.
- (21) Janell, D.; Tocilj, A.; Kölln, I.; Schlünzen, F.; Glühmann, M.; Hansen, H. A. S.; Harms, J.; Bashan, A.; Agmon, I.; Bartels, H.; Kessler, M.; Weinstein, S.; Franceschi, F.; Yonath, A. Ribosomal Crystallography and Heteropolytungstates. In *Polyoxometalate Chemistry From Topology via Self-Assembly to Applications*; Springer: Dordrecht, 2006. pp. 391–415. DOI: [10.1007/0-306-47625-8_25](https://doi.org/10.1007/0-306-47625-8_25)
- (22) Blazevic, A.; Rompel, A. The Anderson-Evans Polyoxometalate: From Inorganic Building Blocks via Hybrid Organic-Inorganic Structures to Tomorrows “Bio-POM”. *Coord. Chem. Rev.* **2016**, *307*, 42–64.
- (23) Herrmann, S.; Seliverstov, A.; Streb, C. Polyoxometalate-Ionic Liquids (POM-ILs)—The Ultimate Soft Polyoxometalates? A Critical Perspective. *J. Mol. Eng. Mater.* **2014**, *02*, No. 1440001.
- (24) Buffet-Bataillon, S.; Tattevin, P.; Bonnaure-Mallet, M.; Jolivet-Gougeon, A. Emergence of Resistance to Antibacterial Agents: The Role of Quaternary Ammonium Compounds—A Critical Review. *Int. J. Antimicrob. Agents* **2012**, *39*, 381–389.
- (25) Herrmann, S.; De Matteis, L.; De La Fuente, J. M.; Mitchell, S. G.; Streb, C. Removal of Multiple Contaminants from Water by Polyoxometalate Supported Ionic Liquid Phases (POM-SILPs). *Angew. Chem., Int. Ed.* **2017**, *56*, 1667–1670.
- (26) Misra, A.; Zambrzycki, C.; Kloker, G.; Kotyrba, A.; Anjass, M.; Castillo, I.; Mitchell, S.; Guttel, R.; Streb, C. Water Purification and Microplastics Removal Using Magnetic Polyoxometalate Supported-Ionic Liquid Phases (MagPOM-SILPs). *Angew. Chem., Int. Ed.* **2020**, *59*, 1601–1605.
- (27) Ma, T.; Yang, P.; Dammann, I.; Lin, Z.; Mougharbel, A. S.; Li, M.; Ada, F.; Mitea, R.; Silvestru, C.; Thorstenson, C.; Ullrich, M. S.; Cseh, K.; Jakupc, M. A.; Keppler, B. K.; Donalisio, M.; Cavalli, R.; Lembo, D.; Kortz, U. Tetra-(p-tolyl)antimony(III)-Containing Heteropolytungstates, $\left[\left(p\text{-Tolyl}\right)\text{Sb}^{\text{III}}\right]_4 \left(\text{A}-\alpha\text{-XW}_9\text{O}_{34}\right)_2\right]^{n-}$ ($\text{X} = \text{P}$, As , or Ge): Synthesis, Structure, and Study of Antibacterial and Antitumor Activity. *Inorg. Chem.* **2020**, *59*, 2978–2987.

- (28) Kibler, A. J.; Martín, C.; Cameron, J. M.; Rogalska, A.; Dupont, J.; Walsh, D. A.; Newton, G. N. Physical and Electrochemical Modulation of Polyoxometalate Ionic Liquids via Organic Functionalization. *Eur. J. Inorg. Chem.* **2019**, *2019*, 456–460.
- (29) Amir, M. K.; Khan, S.; Zia-Ur-Rehman; Shah, A.; Butler, I. S. Anticancer Activity of Organotin(IV) Carboxylates. *Inorganica Chim. Acta* **2014**, *423*, 14–25.
- (30) Tabassum, S.; Pettinari, C. Chemical and Biotechnological Developments in Organotin Cancer Chemotherapy. *J. Organomet. Chem.* **2006**, *691*, 1761–1766.
- (31) Carraher, C. E.; Roner, M. R. Organotin Polymers as Anticancer and Antiviral Agents. *J. Organomet. Chem.* **2014**, *751*, 67–82.
- (32) Xin, F.; Pope, M. T.; Long, G. J.; Russo, U. Polyoxometalate Derivatives with Multiple Organic Groups. 2. Synthesis and Structures of Tris(Organotin) α,β -Keggin Tungstosilicates. *Inorg. Chem.* **1996**, *35*, 1207–1213.
- (33) Haraguchi, N.; Okaue, Y.; Isobe, T.; Matsuda, Y. Stabilization of Tetravalent Cerium upon Coordination of Unsaturated Heteropoly Tungstate Anions. *Inorg. Chem.* **1994**, *33*, 1015–1020.
- (34) System, B. A. X.; SAINT Plus, version 8.34a; Madison, WI, 2013.
- (35) Sheldrick, G. M.; BRUKER-Siemens Area Detect. SADABS.
- (36) Sheldrick, G. M. Crystal structure refinement with SHELXL. *Acta Crystallogr., Sect. C: Struct. Chem.* **2015**, *71*, 3–8.
- (37) Sheldrick, G. M. A short history of SHELX. *Acta Crystallogr., Sect. A: Found. Crystallogr.* **2008**, *64*, 112–122.
- (38) Dolomanov, O. V.; Bourhis, L. J.; Gildea, R. J.; Howard, J. A. K.; Puschmann, H. OLEX2: a complete structure solution, refinement, and analysis program. *J. Appl. Crystallogr.* **2009**, *42*, 339–341.
- (39) SCALE3 ABSPACK - An Oxford Diffraction program (1.0.4.gui:1.0.3); Oxford Diffraction Ltd., 2005.
- (40) Ilavsky, J.; Jemian, P. R. Irena: Tool Suite for Modeling and Analysis of Small-Angle Scattering. *J. Appl. Crystallogr.* **2009**, *42*, 347–353.
- (41) Zhang, R.; Thiagarajan, P.; Tiede, D. M. Probing Protein Fine Structures by Wide Angle Solution X-Ray Scattering. *J. Appl. Crystallogr.* **2000**, *33*, 565–568.
- (42) Nečas, D.; Klapetek, P. Gwyddion: An Open-Source Software for SPM Data Analysis. *Cent. Eur. J. Phys.* **2012**, *10*, 181–188.
- (43) Rickert, P. G.; Antonio, M. R.; Firestone, M. A.; Kubatko, K. A.; Szreder, T.; Wishart, J. F.; Dietz, M. L. Tetraalkylphosphonium Polyoxometalate Ionic Liquids: Novel, Organic-Inorganic Hybrid Materials. *J. Phys. Chem. B* **2007**, *111*, 4685–4692.
- (44) Gameiras, J. A.; Couto, F. A. S.; Trovão, M. C. N.; Cavaleiro, A. M. V.; Cavaleiro, J. A. S.; De Jesus, J. D. P. Investigation of the Thermal Decomposition of Some Metal-Substituted Keggin Tungstophosphates. *Thermochim. Acta* **1999**, *326*, 165–173.
- (45) Maksimovskaya, R. I. Hydrolysis of Heteropoly Acid $H_3PW_{12}O_{40}$ by ^{31}P NMR. *Zhurn. Neorg. Khim.* **1998**, *43*, 1960–1972.
- (46) Maksimovskaya, R. I.; Maksimov, G. M. ^{31}P NMR Studies of Hydrolytic Conversions of 12-Tungstophosphoric Heteropolyacid. *Coord. Chem. Rev.* **2019**, *385*, 81–99.